Improved modeling of relativistic collisions and collisional ionization in particle-in-cell codes

F. Pérez, L. Gremillet, A. Decoster, M. Drouin, and E. Lefebvre

Related Articles

Additional information on Phys. Plasmas
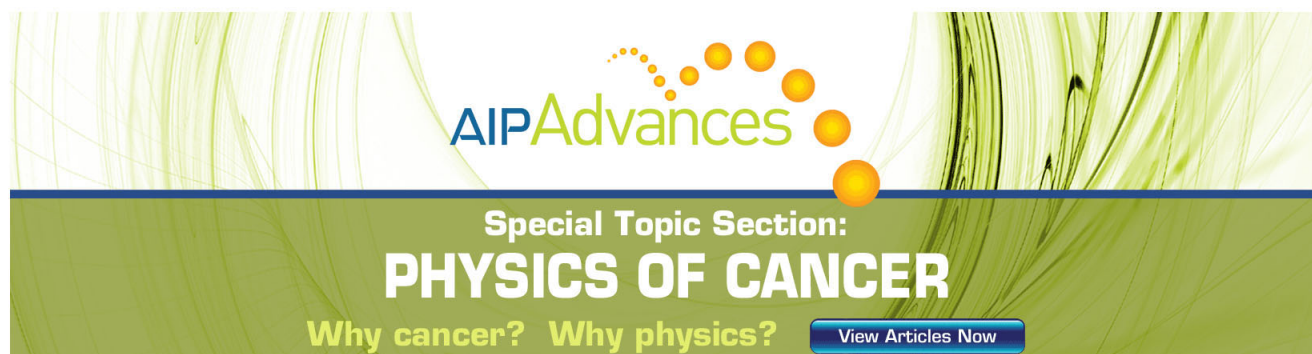
Improved modeling of relativistic collisions and collisional ionization in particle-in-cell codes

F. Pérez,[1,2,a)] L. Gremillet,[2,b)] A. Decoster,[2] M. Drouin,[2] and E. Lefebvre[2]
[1]*LULI, Ecole Polytechnique, 91128 Palaiseau Cedex, France*
[2]*CEA, DAM, DIF, F-91297 Arpajon, France*

An improved Monte Carlo collisional scheme modeling both elastic and inelastic interactions has been implemented into the particle-in-cell code CALDER [E. Lefebvre *et al.*, Nucl. Fusion **43**, 629 (2003)]. Based on the technique proposed by Nanbu and Yonemura [J. Comput. Phys. **145**, 639 (1998)] allowing to handle arbitrarily weighted macro-particles, this binary collision scheme uses a more compact and accurate relativistic formulation than the algorithm recently worked out by Sentoku and Kemp [J. Comput. Phys. **227**, 6846 (2008)]. Our scheme is validated through several test cases, demonstrating, in particular, its capability of modeling the electrical resistivity and stopping power of a solid-density plasma over a broad parameter range. A relativistic collisional ionization scheme is developed within the same framework, and tested in several physical scenarios. Finally, our scheme is applied in a set of integrated particle-in-cell simulations of laser-driven fast electron transport. © *2012 American Institute of Physics*. [http://dx.doi.org/10.1063/1.4742167]

I. INTRODUCTION

Realistic numerical simulations of the interaction between ultra-intense laser pulses and dense materials require accurate modeling of the intertwined collisional and collective processes induced by the laser-driven fast particles. For instance, the energy deposition and field generation by the relativistic electrons accelerated into solid-density targets by lasers pulses of intensities above 10^{18} W/cm^2 underlie many applications ranging from the production of warm dense matter[1,2] and the fast-ignition concept for inertial confinement fusion[3] to ion acceleration[4] and positron generation.[5] Many aspects of the highly nonlinear transport physics at play in these various scenarios need further understanding in order to reach a predictive modeling capability.

Particle-in-cell (PIC) codes have become widely used simulation tools for describing the short-time-scale evolution of plasmas subjected to intense electromagnetic waves or charged particle beams.[6] They account for the reciprocal interactions between charged particles and self-consistent electromagnetic fields by means of a combined Lagrangian-Eulerian scheme. Recent progresses in parallel computing have now made it possible to simulate two-dimensional solid-density samples of experimentally relevant dimensions ($\sim 50 \times 50\ \mu$m^2) over a typical duration of 1 ps.[2,7] However, since PIC simulations are usually run with mesh sizes larger than the Debye length, they do not address self-consistently the collisional effects expected to influence, directly or indirectly, the transport of intense particle beams through dense materials.

Monte Carlo algorithms modeling elastic binary collisions were introduced decades ago in nonrelativistic plasma simulations using equally weighted macro-particles.[8,9] The

relativistic regime was first addressed by Wallace *et al.*[10] within a simplified approach accounting for electron deflections only. Later on, it was dealt with more accurately by Sentoku and Kemp,[11] most notably to manage arbitrarily weighted particles and high-density effects. More recently, Peano *et al.*[12] developed a general procedure for the sampling of particle pairs which ensures physical consistency in the ultra-relativistic limit.

The goal of the present article is to develop an improved relativistic collision scheme modeling both elastic and inelastic interactions, and its implementation within the existing PIC code CALDER.[13] As in Ref. 11, special emphasis is put on high-density effects. Our algorithm makes use of the Monte Carlo model developed by Nanbu,[14,15] which allows for relatively large time-steps[16] and weighted particles. Our method differs from Ref. 11 in providing a more straightforward relativistic formulation, as well as an alternate low-temperature correction of the collision rate. Likewise, our collisional ionization scheme extends to the relativistic regime and weighted particles the scheme introduced by Kemp *et al.*,[17] in addition to describing more accurately the energy transfers between incident and secondary particles.

This paper is organized as follows. The elastic collision scheme is detailed in Sec. II and validated in Sec. III through several test cases. The ionization model is presented in Sec. IV and tested in Sec. V. Section VI is devoted to integrated simulations illustrating the changes entailed by collisional processes. Finally, our results are summarized in Sec. VII.

II. ELASTIC COLLISION SCHEME

A. Elementary collision process

Let us first consider the Coulomb interaction between a test particle from species 1 and a population of particles from species 2. Species 1 and 2 are defined by their respective electrical charges q_1 and q_2, masses m_1 and m_2, and number

---

densities n_1 and n_2. In the laboratory frame, their momenta are $\mathbf{p}_1$ and $\mathbf{p}_2$, velocities $\mathbf{v}_1$ and $\mathbf{v}_2$, and Lorentz factors γ_1 and γ_2, respectively. Following the line of Ref. 18, it proves convenient to perform the collision within the center-of-mass (CM) frame whose velocity is

$$\mathbf{v}_C = \frac{\mathbf{p}_1 + \mathbf{p}_2}{m_1 \gamma_1 + m_2 \gamma_2}. \tag{1}$$

In the CM frame, where variables are denoted by a star ($\star$), the Lorentz-transformed momentum of the test particle writes[11]

$$\mathbf{p}_1^\star = \mathbf{p}_1 + \left[\frac{\gamma_C - 1}{v_C^2} (\mathbf{v}_C \cdot \mathbf{v}_1) - \gamma_C \right] m_1 \gamma_1 \mathbf{v}_C, \tag{2}$$

where $\gamma_C = (1 - v_C^2/c^2)^{-1/2}$ and c is the speed of light. By definition of the CM frame, we have $\mathbf{p}_1^\star = -\mathbf{p}_2^\star$, and the collision reduces to a rotation.

In order to allow for computation time-steps much larger than the single-collision time, we need a theoretical framework for calculating the cumulative deviation angle $\chi^\star$ ($0 \leq \chi^\star \leq \pi$) of the test particle after N successive small-angle collisions. In the following, we shall employ the cumulative-angle distribution derived by Nanbu[14]

$$f(\chi^\star) = \frac{A}{4\pi \sinh A} \exp(A \cos \chi^\star), \tag{3}$$

the quantity $2\pi f(\chi^\star) \sin \chi^\star d\chi^\star$ being defined as the probability for a cumulative deviation between $\chi^\star$ and $\chi^\star + d\chi^\star$. The factor A is a solution of the nonlinear equation

$$\coth A - A^{-1} = \exp(-s_{12}). \tag{4}$$

This distribution function (Eq. (3)) is controlled by a single parameter $s_{12} = N\langle \theta^{\star 2} \rangle/2$, where $\langle \theta^{\star 2} \rangle$ is the mean-squared scattering angle for a single collision. An accurate relativistic calculation of s_{12} is worked out in the following.

By definition of the effective collisional cross-section σ, the number of collisions is $N = \sigma v_{\mathrm{rel}} n_2 \Delta t$, where $v_{\mathrm{rel}} = |\mathbf{v}_1 - \mathbf{v}_2|$. Making use of the relativistic invariant $\sigma v_{\mathrm{rel}} \gamma_1 \gamma_2$,[19] there follows:

$$N = \sigma^\star v_{\mathrm{rel}}^\star \frac{\gamma_1^\star \gamma_2^\star}{\gamma_1 \gamma_2} n_2 \Delta t. \tag{5}$$

The relativistic differential Coulomb-scattering cross-section has been calculated in the CM frame by Frankel *et al.*[20] and reads

$$\frac{d\sigma^\star}{d\Omega^\star} = \left(\frac{2 q_1 q_2}{4\pi \epsilon_0} \frac{1 + v_1^\star v_2^\star / c^2}{p_1^\star v_{rel}^\star} \right)^2 \frac{1}{\theta^{\star 4}}. \tag{6}$$

Integrating this expression from $\theta_{\min}$ (corresponding to an impact parameter equal to the Debye length) to $\theta_{\max} = 2$ rad, as prescribed in Ref. 20, gives the statistical expectation

$$\langle \theta^{\star 2} \rangle = \frac{1}{\sigma^\star} \frac{\ln\Lambda}{2\pi} \left(\frac{q_1 q_2}{\epsilon_0} \frac{1 + v_1^\star v_2^\star / c^2}{p_1^\star v_{\mathrm{rel}}^\star} \right)^2, \tag{7}$$

where we have introduced the Coulomb logarithm $\ln\Lambda = \ln(2/\theta_{\min})$. Upon combining Eqs. (5) and (7), substituting the Lorentz transforms $\gamma_1^\star = (1 - \mathbf{v}_C \cdot \mathbf{v}_1/c^2)\gamma_C \gamma_1$ and $\gamma_2^\star = (1 - \mathbf{v}_C \cdot \mathbf{v}_2/c^2)\gamma_C \gamma_2$, and expressing

$$v_{\mathrm{rel}}^\star = v_1^\star + v_2^\star = \frac{(m_1 \gamma_1 + m_2 \gamma_2)p_1^\star}{m_1 \gamma_1^\star m_2 \gamma_2^\star \gamma_C}, \tag{8}$$

one obtains the relativistic expression of s_{12}

$$s_{12} = \frac{n_2 \Delta t \ln\Lambda (q_1 q_2)^2}{4\pi \epsilon_0^2 c^4 m_1 \gamma_1 m_2 \gamma_2} \frac{\gamma_C p_1^\star}{m_1 \gamma_1 + m_2 \gamma_2}$$
$$\times \left(\frac{m_1 \gamma_1^\star m_2 \gamma_2^\star}{p_1^{\star 2}} c^2 + 1 \right)^2. \tag{9}$$

Given a random number $U \in [0;1]$, the scattering angle $\chi^\star$ is given by the standard inversion sampling method

$$\cos \chi^\star = A^{-1} \ln(e^{-A} + 2U \sinh A). \tag{10}$$

Its computation is split into the following cases:

1. If $s_{12} < 0.1$ then $\cos \chi^\star = 1 + s_{12} \ln U$.
2. If $0.1 < s_{12} < 3$ then

$$A^{-1} = 0.0056958 + 0.9560202\, s_{12} - 0.508139\, s_{12}^2$$
$$+ 0.47913906\, s_{12}^3 - 0.12788975\, s_{12}^4$$
$$+ 0.02389567\, s_{12}^5 \tag{11}$$

3. If $3 < s_{12} < 6$ then $A = 3\exp(-s_{12})$.
4. If $6 < s_{12}$ then $\cos \chi^\star = 2U + 1$.

Note that the polynomial fit of case 2 allows for a computation 30% faster than the tabulation technique suggested in Ref. 14. After randomly choosing the azimuthal angle $\phi^\star \in [0; 2\pi]$, the following rotational transform[11] gives the resulting momentum $\mathbf{p}_{1f}^\star$ of the test particle

$$\mathbf{p}_{1f}^\star = -\mathbf{p}_{2f}^\star = \begin{bmatrix} \dfrac{p_{1x}^\star p_{1z}^\star}{p_{1\perp}^\star} & -\dfrac{p_{1y}^\star p_1^\star}{p_{1\perp}^\star} & p_{1x}^\star \\[2ex] \dfrac{p_{1y}^\star p_{1z}^\star}{p_{1\perp}^\star} & \dfrac{p_{1x}^\star p_1^\star}{p_{1\perp}^\star} & p_{1y}^\star \\[2ex] -p_{1\perp}^\star & 0 & p_{1z}^\star \end{bmatrix} \cdot \begin{pmatrix} \sin \chi^\star \cos \phi^\star \\ \sin \chi^\star \sin \phi^\star \\ \cos \chi^\star \end{pmatrix}, \tag{12}$$

where $p_{1\perp}^\star = \sqrt{p_{1x}^{\star 2} + p_{1y}^{\star 2}}$. Finally, the particle momentum is computed in the lab frame[11]

$$\mathbf{p}_{1f} = \mathbf{p}_{1f}^\star + \mathbf{v}_C \left[\frac{\gamma_C - 1}{v_C^2} (\mathbf{v}_C \cdot \mathbf{p}_{1f}^\star) + m_1 \gamma_1^\star \gamma_C \right]. \tag{13}$$

To summarize this section, we have derived the momentum change undergone during a time step Δt by a relativistic

test particle colliding with a population of charged particles. Our calculation is performed in the CM frame only, in contrast to that of Ref. 11, which alternates between the CM frame and the rest frame of one of the particles (OPR). Note that, in that work, the relativistic changes in the density and the time-step are neglected when expressing the angular variance (which is equivalent to the parameter s_{12} in the OPR frame,[21] hence resulting in a missing factor $1 - \mathbf{v}_1 . \mathbf{v}_2 / c^2$. The error due to this inconsistency is negligible provided at least one of the colliding particles is nonrelativistic in the lab frame.

B. Numerical implementation for arbitrarily weighted macro-particles

Most modern PIC codes make use of macro-particles of varying numerical weights when simulating strongly inhomogeneous plasmas or wave-particle processes (e.g., beam-plasma instabilities) localized in the phase space. The above theory must then be adapted to such numerical configurations. To this goal, let us consider the collisions occurring within a given mesh cell (usually taken of the order, or larger than the Debye length) between two populations containing, respectively, N_1 and N_2 macro-particles from species 1 and 2, and of individual weights W_{i1} and W_{i2}. The index $i \in [1; N_{12}]$ randomly associates pairs of colliding macro-particles, where $N_{12} = \max(N_1, N_2)$ is the total number of pairs (the process for choosing pairs is described by Nanbu and Yonemura[15]). As the weight corresponds to the number of real particles represented by one macro-particle, the local number densities of those two populations are $n_1 = \sum_{i=1}^{N_1} W_{i1}$ and $n_2 = \sum_{i=1}^{N_2} W_{i2}$.

For each *macro*-collision, the Monte Carlo scheme consists in associating with the two interacting macro-particles the local density of their respective species. Equations (2)–(13) can thus be applied in order to obtain the resulting momenta of both macro-particles. However, as we adopted the point of view of species 1, Eq. (9) is not symmetric upon the species. Nanbu and Yonemura[15] solved this problem through the following reasoning, based on the effective interaction time-step experienced by each macro-particle. One macro-collision may be viewed as $\min(W_{i1}, W_{i2})$ collisions between real particles. This implies that the macro-particle of smallest weight undergoes the right number of collisions, while the other one collides *too much*. The latter must then be allowed to collide only with a finite probability in order to fix the asymmetry. In general, we can write this probability

$$P_{i1} = \frac{W_{i2}}{\max(W_{i1}, W_{i2})} \quad \text{and} \quad P_{i2} = \frac{W_{i1}}{\max(W_{i1}, W_{i2})}, \quad (14)$$

for the first and second macro-particles, respectively. This so-called rejection method, commonly used in Monte Carlo codes,[22] implicitly modifies the effective time-increment of each macro-particle as $\delta t_{i1} = P_{i1} \Delta t_1$ and $\delta t_{i2} = P_{i2} \Delta t_2$, respectively, where the Δt_α denotes the time-step associated with real particles. Now, the average time-increment per real particle 1 is

$$\overline{\Delta t_1} = \frac{\sum_{i=1}^{N_{12}} W_{i1} \delta t_{i1}}{\sum_{i=1}^{N_1} W_{i1}} = \Delta t_1 \frac{\sum_{i=1}^{N_{12}} W_{i1} P_{i1}}{n_1} = \Delta t_1 \frac{n_{12}}{n_1}, \quad (15)$$

where

$$n_{12} = \sum_{i=1}^{N_{12}} \min(W_{i1}, W_{i2}). \quad (16)$$

Similarly, we have $\overline{\Delta t_2} = \Delta t_2 n_{12}/n_2$. Finally, requiring equal average time-increments $\overline{\Delta t_1} = \overline{\Delta t_2} = \overline{\Delta t}$ (where $\overline{\Delta t}$ is the computing time-step), one obtains a common value

$$s = s_{12}(\Delta t_1) = s_{21}(\Delta t_2) = \frac{n_1 n_2}{n_{12}} \frac{\overline{\Delta t} \ln \Lambda (q_1 q_2)^2}{4\pi \epsilon_0^2 c^4 m_1 \gamma_1 m_2 \gamma_2}$$

$$\times \frac{\gamma_C p_1^\star}{m_1 \gamma_1 + m_2 \gamma_2} \left(\frac{m_1 \gamma_1^\star m_2 \gamma_2^\star}{p_1^{\star 2}} c^2 + 1 \right)^2. \quad (17)$$

This method ensures that, for a large enough number of particles, the energy and momentum are conserved on average. To assess its accuracy in a scenario of interest in the context of laser-solid interaction (see Sec. VI), we have simulated the purely collisional evolution of a one-dimensional, solid Al^{6+} Maxwellian plasma with $T_e = T_i = 100 \, \text{eV}$, discretized over 128 cells. We have used an equal number, N_c, of ions and electrons per cell, hence $W_e / W_i = 6$. While the total energy is found to be well conserved for N_c values as low as 10, the overall trend (not shown) is that of nonphysical ion heating and electron cooling. Yet, a rather modest value $N_c \geq 50$ suffices to ensure tolerable ion and electron energy variations (lower than 6% and 1%, respectively) over a ~ 0.5-ps timespan. In the case of a nonequilibrium plasma with $T_e = 1000 \, \text{eV}$ and $T_i = 100 \, \text{eV}$, we have checked that the results obtained with $N_c = 50$ and $N_c = 500$ agree within a $\sim 2\%$ error.

C. Low-temperature correction

Equation (17) assumes an ideal plasma (i.e., pertaining to the Spitzer regime), and thus becomes invalid in a low-temperature dense plasma (typically for temperatures $< 100 \, \text{eV}$ at solid density) since it predicts a mean free path lower than the mean interatomic distance. As this is not physically acceptable, let us follow Lee and More's heuristic approach[23] (see also Ref. 24) and limit the collision frequency so that the mean free path as seen by both populations remains larger than the mean distance between the target particles, i.e., $\lambda_1 \geq (4\pi n_2/3)^{-1/3}$ and $\lambda_2 \geq (4\pi n_1/3)^{-1/3}$. Degeneracy effects are here neglected as they arise at lower temperatures (i.e., below the Fermi temperature). Since the collision frequencies $\nu_{12} = v_{\text{rel}}/\lambda_1$ and $\nu_{21} = v_{\text{rel}}/\lambda_2$ are related to each other according to $m_1 n_1 \nu_{12} = m_2 n_2 \nu_{21}$,[25] the above inequalities can be reduced to

$$\lambda_1 \geq \left(\frac{3}{4\pi} \right)^{1/3} \frac{\max(m_1 n_1^{2/3}, m_2 n_2^{2/3})}{m_2 n_2}. \quad (18)$$

Furthermore, in the non-relativistic limit relevant for the coupled-plasma regime, the parameter s from Eq. (17) becomes

$$s = \frac{n_1 n_2}{n_{12}} \frac{\overline{\Delta t} \ln\Lambda (q_1 q_2)^2}{4\pi\epsilon_0^2 m_{12}^2} \frac{1}{v_{\mathrm{rel}}^3}, \quad (19)$$

where $m_{12}^{-1} = m_1^{-1} + m_2^{-1}$ and v_{rel} can be assimilated to $v_{\mathrm{rel}}^\star$ given by Eq. (8). By comparing this expression to the well-known formula of the nonrelativistic collision frequency ν_{12} between a particle of species 1 and a drifting population of species 2 (see Ref. 25), one obtains

$$s = \frac{n_1 m_1}{n_{12} m_{12}} \nu_{12} \overline{\Delta t} = \frac{n_1 m_1}{n_{12} m_{12}} \frac{v_{\mathrm{rel}}}{\lambda_1} \overline{\Delta t}. \quad (20)$$

The lower bound of λ_1 from Eq. (18) thus implies the following upper bound for s:

$$s' = \left(\frac{4\pi}{3}\right)^{1/3} \frac{n_1 n_2}{n_{12}} \overline{\Delta t} \frac{m_1 + m_2}{\max(m_1 n_1^{2/3}, m_2 n_2^{2/3})} v_{\mathrm{rel}}. \quad (21)$$

One may simply replace the quantity s by $\min(s, s')$ in order to extend the above results to arbitrary temperatures.

D. Varying Coulomb logarithm

The Coulomb logarithm involved in Eq. (17) can be computed from the formulae given in Ref. 23. First, the Debye length of the whole plasma (i.e., the maximum impact parameter) is computed by summing over the different species: $\lambda_D^{-2} = \sum_{\alpha=1,2} 4\pi n_\alpha q_\alpha^2 / T_\alpha$, where T_α is the temperature of each species. Note that the Debye length is constrained to be higher than the minimum mean interatomic distance $r_{\min} = (4\pi n_{\max}/3)^{-1/3}$, where $n_{\max}$ is the maximum density amongst the species under consideration. Second, the minimum impact parameter is $b_{\min} = \max(h/2p^\star, b_0)$, where

$$b_0 = \frac{q_1 q_2}{4\pi\epsilon_0 c^2} \frac{\gamma_C}{m_1\gamma_1 + m_2\gamma_2} \left(\frac{m_1\gamma_1^\star m_2\gamma_2^\star}{p_1^{\star 2}} c^2 + 1\right)^2 \quad (22)$$

is the impact parameter corresponding to a 2 rad deviation angle (see Ref. 20). The resulting Coulomb logarithm is given by

$$\ln\Lambda = \max\left[2, \frac{1}{2}\ln\left(1 + \frac{\lambda_D^2}{b_{\min}^2}\right)\right], \quad (23)$$

where the lower bound $\ln\Lambda = 2$ is introduced in Ref. 23 so as to agree with numerical results. The Coulomb logarithm is computed for each collision, but λ_D is common to all collisions performed in a given cell.

III. NUMERICAL TESTS OF THE ELASTIC COLLISION SCHEME

A. Electrical conductivity

As a first test of the Monte Carlo collision scheme described above, the electrical conductivity σ_{Cu} of solid-

density copper at thermal equilibrium is simulated for a set of temperatures T between 1 and 1000 eV. In each case, the input ionization state $Z^\star$ and electron density n_e are calculated from a modified Thomas-Fermi model.[26] The simulations are one-dimensional in space, 250 μm-long, using 1 μm-wide cells, each containing 40 000 particles of each kind. The timestep is set to $\Delta t = 2.5 \times 10^{-3}$ fs. The self-consistent electric field resulting from Poisson's equation is suppressed in these simulations. Instead, a constant electric field $E_x = 3 \times 10^9$ V/m is applied: electrons are accelerated and then slowed down by collisions. Generation of runaway electrons is negligible since E_x is always well below the Dreicer field $E_c \sim e^3 n_e/(2\pi\epsilon_0^2 k_B T)$, which ranges from 10^{10} to 10^{13} V/m here. The asymptotic electron drift velocity v_f is related to the conductivity by $\sigma_{\mathrm{Cu}} = -e\, n_e v_f / E_x$. The time history of the drift velocity $v_d(t)$ thus provides a direct estimate of the electrical conductivity. However, as illustrated in Fig. 1 for varying plasma temperatures, $|v_d(t)|$ slowly increases at late times due to ohmic heating: the electron temperature continuously rises and so does the conductivity in the Spitzer regime. We have found that $v_d(t)$ can be satisfactorily fitted to a function of the form

$$v_d(t) \approx A\, t + v_f(1 - \exp(-t/\tau)), \quad (24)$$

with the fitting parameters v_f, A, and τ.

The conductivity σ_{Cu} inferred from the best-fitting value of v_f is plotted in Fig. 2 as a function of the initial electron temperature T (squares). For temperatures above 50 eV, the Spitzer conductivity is well reproduced. Below 50 eV, a well-known saturation occurs due to the lower bound imposed on the mean free path.[23,24]

The validity of our computation can be first checked by comparing it to the analytical formula[23]

$$\sigma_{\lim} = \frac{e^2}{3} \int \lambda(v) v \frac{\partial f_0}{\partial\epsilon} d^3 p, \quad (25)$$

where the electron energy distribution is chosen to be Maxwellian $f_0(\epsilon) = n_e(2\pi m_e kT)^{-3/2}\exp(-\epsilon/kT)$. Consistently with the discussion of Sec. II C, we take the mean free path as
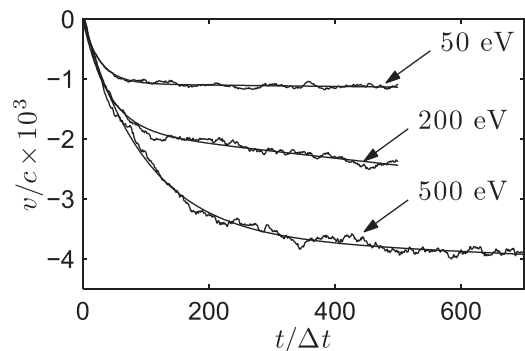

FIG. 1. Mean electron velocity vs time in a Cu plasma subjected to a constant electrostatic field for three different initial temperatures. Exponential fits of the form (24) are also plotted.
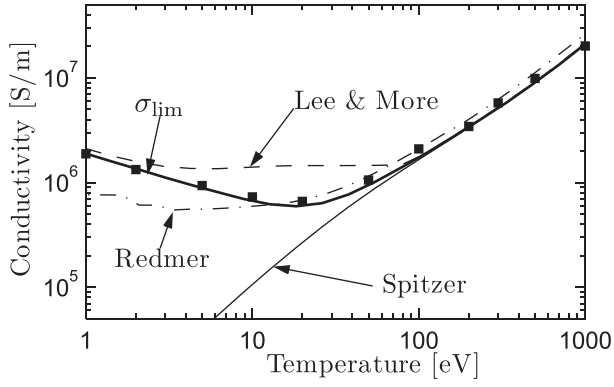
FIG. 2. Electrical conductivity of solid-density copper vs temperature as inferred from the Monte Carlo scheme (squares) and compared to various models.

$\lambda(v) = \max(\lambda_{sp}(v), d)$, with $\lambda_{sp}(v) = 4\pi\epsilon_0^2 m_e^2 v_f^4/(Z^{\star 2} e^4 n_i \ln\Lambda)$ and $d = (4\pi n_i/3)^{-1/3}$. This integral has a closed-form solution, hence leading to the low-temperature-corrected conductivity

$$\sigma_{lim} = \frac{8\pi\epsilon_0 c}{r_e} \left[\frac{2Z^\star}{3\pi\bar{l}^2 \sqrt{\bar{T}_e}} [1 - (1+a)e^{-a}] \right.$$
$$\left. + \frac{\bar{T}_e^{3/2}}{Z^\star \ln\Lambda} \left(1 + a + \frac{a^2}{2} + \frac{a^3}{6}\right) e^{-a} \right], \qquad (26)$$

where r_e is the classical electron radius. We have introduced the normalized temperature $\bar{T}_e = 2kT/(\pi m_e c^2)$ and interatomic distance $\bar{l} = (n_i r_e^3 \sqrt{3/4\pi})^{-1/3}$, as well as the dimensionless parameter $a = 2Z^\star(\ln\Lambda/\pi)^{1/2}/(\bar{l}\bar{T}_e)$. Equation (26) contains two terms associated with the low-temperature limit, proportional to $T^{-1/2}$, and Spitzer's limit, proportional to $T^{3/2}$, respectively. This expression is compared to the simulation results in Fig. 2. A good agreement is obtained at both high and low temperatures.

A comparison to the original Lee and More's model[23] is provided in the same graph. The slight discrepancy visible at low temperatures stems from different implementations of the lower bound on the mean free path: Lee and More apply the low-temperature limit on the average value of λ, whereas it is done in each collision in our Monte Carlo scheme. For the sake of completeness, our results are confronted to the more sophisticated calculation of Redmer,[27] based on a linear response theory formalism. The agreement is, of course, not perfect, yet the general behavior is correctly reproduced.

Overall, the electrical conductivity resulting from our Monte Carlo scheme has been validated in a broad temperature range covering the ideal and coupled plasma regimes. Our scheme, therefore, allows for quantitative PIC simulations of dense plasmas subjected to intense laser fields and particle currents wherein, as illustrated in Sec. VI A, the electrical conductivity is a major parameter determining the strength of quasistatic fields.[7,28]

B. Elastic stopping power

As a first simple case study, the slowing down of test electrons by elastic $e - i$ collisions is addressed in the relativistic regime. To this goal, let us consider a fast electron beam
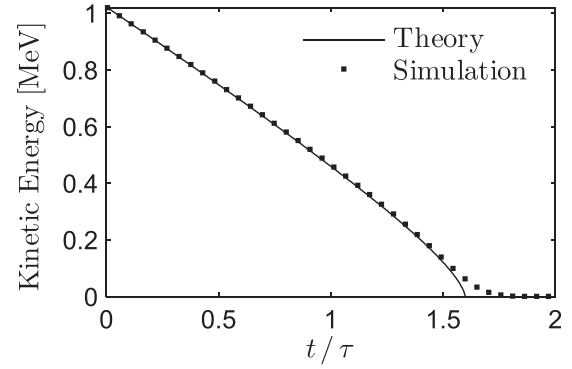

FIG. 3. Slowing down of 1 MeV test electrons through an initially cold ion plasma: comparison between simulation (dots) and theory [Eq. (27)] (solid line).

colliding with initially cold target ions. The fields' effects are suppressed here. Assuming fixed ions, the evolution of the beam's mean momentum p should obey the following formula:[29]

$$\arctan(p) - p - \arctan(p_0) + p_0 = \frac{t}{\tau}, \qquad (27)$$

where $\tau = \frac{4\pi\epsilon_0^2 m_e m_i c^3}{q_e^2 q_i^2 n_i \ln\Lambda}$ and p_0 is the initial beam momentum.

Artificially light ions ($m_i = 5m_e$) are employed for a faster computation. They are kept from heating up significantly by using a very low beam density (i.e., $n_e = 10^{-6} n_i$). For accurate statistics, 100 000 electrons and ions are set in this simulation. The initial beam energy was varied from 1 keV to 100 MeV and the subsequent slowing down was observed to be always in very good agreement with Eq. (27). This is exemplified in Fig. 3 where the electron kinetic energy is plotted against t/τ for incident 1 MeV electrons. The theoretical curve closely matches the computation as long as p is not too small. This late-time discrepancy stems from the mobile ions used in the simulation: when the electrons get as slow as the ions, Eq. (27) cannot be applied anymore.

Now, let us consider a more realistic case where the stopping power originates from elastic $e - e$ collisions. Two electronic populations, for which the fields' effects have been disabled, are simulated. The first population has a density of $n_e = 780\,n_c$ (where $n_c = 1.1 \times 10^{21}\,\text{cm}^{-3}$ denotes the critical density for a laser wavelength $\lambda_0 = 1\,\mu m$), corresponding to fully ionized solid Al, and a temperature of $T_e = 5\,\text{keV}$. The second one is a thousand times less dense monokinetic electron beam, with an initial energy E_0 varying from 10 keV to 1 GeV. The time-step was changed from 5×10^{-3} to 5×10^2 fs to match this increase in energy. Each population contains 25 000 macro-particles. The Coulomb logarithm is calculated at each time-step as explained in Sec. II D. As expected, the beam energy E decreases linearly with time at the beginning of the simulation, so the stopping power Q can be computed using

$$Q = \left(\frac{dE}{dx}\right)_0 = \frac{1}{v_0}\left(\frac{dE}{dt}\right)_0, \qquad (28)$$

where v_0 is the initial beam velocity. The quantity $Q/\rho\ln\Lambda$, where ρ is the density of solid Al, is plotted in Fig. 4 as a function of E_0.
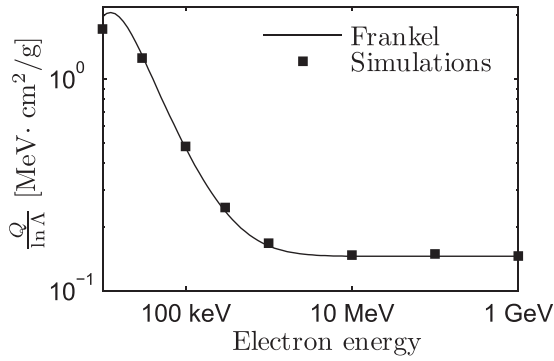
FIG. 4. Energy dependence of the stopping power of beam electrons in Al^{13+} due to elastic $e - e$ collisions with $T_e = 5\,keV$: comparison between PIC simulations (squares) and theory by Frankel *et al.*[20] (solid line).

In the same graph, our simulation results are compared to the theoretical formula of Frankel *et al.*[20]

$$\frac{dE}{dt} = \frac{e^4}{8\pi c\epsilon_0^2} \frac{Z^\star \rho \ln\Lambda}{m_i m_e} \frac{a}{K_2(a)} \int_0^\infty \frac{F(v_1, v_2)}{v_1 v_2 \gamma_1^2 \gamma_2^2} p_2^2 e^{-a\gamma_2} dp_2, \quad (29)$$

where

$$F(v_1, v_2) = (\gamma_1 - \gamma_2)\left[-\frac{A_+ - A_+^2 + 2}{B_+} + \frac{A_- - A_-^2 + 2}{B_-} \right.$$
$$\left. + \ln\left| \frac{A_+ + B_+}{A_- + B_-} \right| \right],$$

$A_\pm = \gamma_1 \gamma_2 (1 \pm v_1 v_2)$, $B_\pm = \sqrt{A_\pm^2 - 1}$, $\quad a = mc^2/kT_e$, $v_1 = \sqrt{1 - (\frac{E_0}{m_e c^2} - 1)^{-2}}$, K_2 is a modified Bessel function of the second kind and $Z^\star$ denotes the ionization state ($Z^\star = 13$ here). We also have the usual relations $v_{1,2} = p_{1,2}/\gamma_{1,2}$ and $\gamma_{1,2} = \sqrt{1 + p_{1,2}^2}$. A good agreement between simulations and Eq. (29) is obtained, which further validates our elastic collision scheme. Note, though, that in the general case of a partially ionized plasma, the stopping power originates from both the free and bound electrons. The contribution of the latter will be dealt with using the impact ionization scheme that is described in Sec. IV.

IV. COLLISIONAL IONIZATION MODEL

The collision algorithm described in Sec. II is equally well-suited to modeling inelastic collisions. Only ionizing electron-ion collisions will be addressed here. The main numerical difficulty lies in accounting for the contributions to the ionization cross-section of all the atomic orbitals. A rigorous, fully stochastic approach would consist in successively sampling the ionized atomic orbital and the corresponding energy-transfer distribution function. Since we expect such a scheme to be heavily time-consuming, we have resorted to a simpler, partly deterministic technique. Our method consists in tabulating, at the beginning of the calculation, the total ionization cross-section (i.e., integrated over all the orbitals) for each ion species, as a function of the incident electron energy and the ionization degree. The averaged values of the energy

lost by the incident electron and the ejection energy of the secondary electron are also computed. Then, for each electron-ion collision, the corresponding cross-section is extracted from these tables, and the ionization probability is computed. In case of ionization, the energy transfer between the incident and ejected electrons is chosen equal to its averaged value. Ions are assumed to be in their ground state (atomic transitions are assumed instantaneous). Compared to the similar approach of Kemp *et al.*,[17] our method accounts for relativistic effects, energy transfers between the incident and secondary electrons as well as contributions from all atomic orbitals. Furthermore, it is adapted to arbitrarily weighted macro-particles.

A. Binding energies

The computation of the ionization cross-section of a target ion in a given ionization state requires the knowledge of the binding energy of each atomic orbital. Let us note Z the atomic number of a given ion, and Z^* its charge. The orbitals are indexed by k from 1 to $Z - Z^*$, and we denote the corresponding binding energy $B_Z^{Z^*}(k)$. The binding energies $B_Z^0(k)$ of many neutral atoms can be found in Refs. 30–32. The ionization energy of the outer orbital $B_Z^{Z^*}(Z - Z^*)$ has been computed for many ionized atoms by Carlson *et al.*[33] According to these authors, the binding energies can be constructed from these two sets of data as follows:

$$B_Z^{Z^*}(k) = B_Z^{Z^*}(Z - Z^*) - B_Z^0(Z - Z^*) + B_Z^0(k). \quad (30)$$

B. Ionization cross-section and energy transfer pre-processing

Given an incident electron energy E and a target atomic orbital with a binding energy $B_k = B_Z^{Z^*}(k)$, an occupation number N_k and a mean kinetic energy U_k, a relativistic formulation of the differential ionization cross-section $d\sigma_k(E)/dW$, where W is the secondary electron energy, is given by Kim *et al.*[34] Let us first define the dimensionless quantities $\varepsilon = E/B_k$, $w = W/B_k$, $\varepsilon' = E/(m_e c^2)$, $b' = B_k/(m_e c^2)$, $u' = U_k/(m_e c^2)$, $\beta_\varepsilon = 1 - (1 + \varepsilon')^{-2}$, $\beta_b = 1 - (1 + b')^{-2}$, and $\beta_u = 1 - (1 + u')^{-2}$. The differential cross-section can be written as

$$\frac{d\sigma_k}{dw} = \sigma_k^0 \left[A_3 f_3(w) + f_2(w) + \frac{2A_2}{\varepsilon - 1} - A_1 f_1(w) \right], \quad (31)$$

where

$$\sigma_k^0 = 2\pi r_e^2 N / [b'(\beta_\varepsilon^2 + \beta_b^2 + \beta_u^2)],$$
$$f_n(w) = (w + 1)^{-n} + (\varepsilon - w)^{-n},$$
$$A_1 = \frac{1}{1 + \varepsilon} \frac{1 + 2\varepsilon'}{(1 + \varepsilon'/2)^2},$$
$$A_2 = \frac{\varepsilon - 1}{2} \frac{b'^2}{(1 + \varepsilon'/2)^2}, \quad \text{and}$$
$$A_3 = \ln\left(\frac{\beta_\varepsilon^2}{1 - \beta_\varepsilon^2} \right) - \beta_\varepsilon^2 - \ln(2b').$$

This crude approximation has very little effect on the cross-section values compared to the required precision.

Analytically integrating Eq. (31) over w yields the ionization cross-section of the kth orbital

$$\sigma_k = \int_0^{(\varepsilon-1)/2} \frac{d\sigma_k}{dw} dw$$
$$= \sigma_k^0 \left[\frac{A_3}{2}\left(1 - \frac{1}{\varepsilon^2}\right) + 1 - \frac{1}{\varepsilon} + A_2 - A_1\ln\varepsilon \right]. \quad (32)$$

The total ionization cross-section is given by $\bar{\sigma} = \sum_k \sigma_k$. Equation (31) can also be integrated to obtain the statistical mean of w

$$\langle w \rangle_k = \frac{1}{\sigma_k} \int_0^{(\varepsilon-1)/2} w\frac{d\sigma_k}{dw} dw$$
$$= \frac{\sigma_k^0}{\sigma_k} \left[\frac{A_3}{2}\frac{(\varepsilon-1)^2}{\varepsilon(\varepsilon+1)} + 2\ln\left(\frac{\varepsilon+1}{2}\right) - \ln\varepsilon + A_2\frac{\varepsilon-1}{4} \right.$$
$$\left. - A_1\left[\ln\varepsilon - (\varepsilon+1)\ln\left(\frac{\varepsilon+1}{2}\right)\right] \right]. \quad (33)$$

Again, summing Eq. (33) over all orbitals gives the average energy transferred to the secondary electron: $\bar{w} = \sum_k \langle w \rangle_k B_k \sigma_k/\bar{\sigma}$. Similarly, one can compute the average energy lost by the incident electron: $\bar{\varepsilon} = \sum_k [\langle w \rangle_k + 1]B_k\sigma_k/\bar{\sigma}$.

At the beginning of the simulation, the quantities $\bar{\sigma}$, $\bar{w}$, and $\bar{\varepsilon}$ are computed and stored for all possible charge states of the initially neutral or ionized atoms, and for a given set of energies E. Later on, they are interpolated during the computation of each collision in order to calculate the ionization frequency, the energy transferred to the new electron, and the incident electron energy loss, respectively. In this respect, our approach is deterministic as averaged quantities are used. The only random event is the occurrence of ionization.

C. Numerical implementation in the case of weighted macro-particles

When an ion collides with a monokinetic electron population characterized by the number density n_e and relative velocity v_{rel}, the ionization frequency is $\nu_i = |v_{rel}|n_e\bar{\sigma}$ (note that the electron's point of view would lead to $\nu_e = |v_{rel}|n_i\bar{\sigma}$). The ionization probability during a time-step $\overline{\Delta t}$ then writes

$$P_{ioniz} = 1 - \exp(-\nu_i\overline{\Delta t}). \quad (34)$$

This probability distribution is readily sampled: an ionization occurs if $P_{ioniz}^i < U$, where U is a random number uniformly distributed over [0;1]. In this case, a new electron is created at the ion location, with an energy $\bar{w}$ in the center-of-mass frame, and a velocity parallel to the direction of the incident electron. Additionally, the incident electron loses the energy $\bar{\varepsilon}$. Note that, in principle, these energy transfers should be applied in the ion rest frame. In practice, however, the latter is assimilated to the center-of-mass frame, for convenience and computing speed.

In the case of unequal weights, the macro-particle of highest weight will effectively experience the ionization pro-

cess with a probability given by Eq. (14). Consequently, the ionization probability (34) must be modified according to the same method as in Eq. (17) so as to obtain

$$P_{ioniz} = 1 - \exp\left(v_{rel}\frac{n_e n_i}{n_{ei}}\bar{\sigma}\overline{\Delta t}\right), \quad (35)$$

which is common to both macro-particles. Here, $n_{ei} = \sum \min(W_e, W_i)$, where the indices e and i refer to the electronic and ionic species, respectively.

Practically, the ionization scheme proceeds as follows:

- If $W_e \geq W_i$, the incident macro-electron loses the energy $\bar{\varepsilon}$ with a probability W_i/W_e. The macro-ion charge is always incremented and a new macro-electron is created.
- If $W_e < W_i$, the macro-ion is ionized with a probability W_e/W_i: its charge is then incremented and a new macro-electron is created. The incident macro-electron is always slowed down.

Note that the creation of new electrons entails a great disparity of energies and numerical weights within the electronic species. According to whether their energy exceeds or not the ionization potential, these secondary electrons may not be able to participate to subsequent ionizing processes of a given ion. Yet, they are taken into account through the factor n_e/n_{ei}, which may result in a severely overestimated ionization frequency. This problem is solved by accounting only for the electrons above the ionization threshold in the computation of n_e/n_{ei}.

In order to quantify the error in the energy conservation caused by the rejection method in a problem typical of laser-solid interaction, we have simulated the evolution of a nonequilibrium, solid Al^{6+} Maxwellian plasma with $T_e = 1000\,eV$ and $T_i = 100\,eV$, subjected to both elastic and inelastic collisions. For an initial particle number $N_c \geq 50$, we have found that the total (kinetic + binding) energy of the system is conserved within a 5% error.

V. TESTS OF THE IONIZATION MODEL

A. Ionization frequency with arbitrary weights

Let us first demonstrate the ability of our scheme to correctly reproduce the theoretical ionization frequency in the case of varying particle weights. Monokinetic $500\,eV$ electrons, at the density $n_e = 10^{21}$ cm^{-3}, are injected through cold and non-ionized solid aluminum. For simplicity, only the first ionization stage is allowed, and the incident electrons are not slowed down. Within such assumptions, one expects the ion charge to increase in time as $n_i = 1 - \exp(-vn_e\sigma t)$, where v is the electron velocity and σ is the first ionization cross-section.

We use $N_i = 400$ ions per cell whereas the number of electrons per cell N_e is varied from 5 to 800, depending on the simulated case. The time-step is set to 5.6×10^{-3} fs and the numerical domain comprises 128 cells. The mean ion charge vs time is plotted for each simulation in Fig. 5. Time is normalized to the inverse laser frequency $\omega_0^{-1} = 0.53\,fs$ for a laser wavelength $\lambda_0 = 1\,\mu m$. Despite distinct W_e/W_i and N_e/N_i ratios, all the numerical curves closely match the
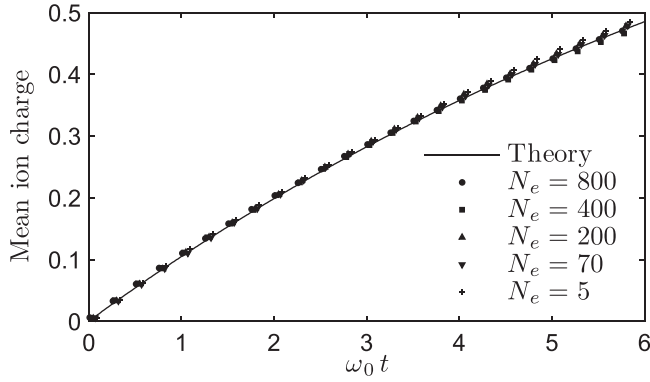
FIG. 5. Time-dependent ionization of solid Al induced by 500 eV monokinetic electrons: comparison between theory[34] and simulations with varying number of macro-electrons per cell N_e.

FIG. 7. Secondary electron density vs time in initially neutral solid Cu due to injection of 2 keV electrons with density $n_e = 10 n_c$. Single-electron ionization alone is modeled. Two time-steps are considered in order to observe the effect of neglected multiple ionization. Time is normalized to $\omega_0^{-1} = 0.53$ fs.

theoretical one. This is made possible by the method detailed in Sec. IV C, which extends, as suggested by Nanbu and Yonemura,[15] the binary collision model to the weighted macro-particle framework.

valid only far above the average ionization potential (~ 160 eV in neutral Al).

C. Multiple ionization

One expects the single-electron ionization approximation to become gradually invalid for increasing time-steps. This is illustrated in Fig. 7 which plots the time-dependent density of secondary electrons generated in solid copper by 2 keV electrons with density $n_e = 10 n_c$. Two values of the time-step are considered, namely, $\Delta t = 0.005 \omega_0^{-1}$ and $0.1 \omega_0^{-1}$. Owing to both numerical and physical constraints, the latter value typically constitutes an upper bound in PIC simulations of solid-density plasmas. The two curves slightly differ, showing that successive single-electron ionizations, negligible for $\Delta t = 0.005 \omega_0^{-1}$, should be accounted for with $\Delta t = 0.1 \omega_0^{-1}$. In the latter case, the ionization rate is of the order of $0.1 \Delta t^{-1}$, hence yielding a significant number of ionization events per time-step. However, the difference between the curves attenuates as the average ion charge rises due to the related decrease in the ionization cross-section (ionized atoms have a higher average ionization potential than their neutral equivalent). Since multiple ionization becomes quickly negligible as the material gets increasingly ionized, we choose to neglect it in CALDER simulations by ensuring a short enough time-step. A similar approach is followed by Ref. 17.

If required, though, multiple ionization can be modeled by adapting the Monte Carlo field ionization scheme recently implemented in CALDER[37] For the sake of simplicity, let us allow for two successive ionizations per time-step only. Introducing $\bar{\sigma}'$ the ionization cross-section after the first ionization (*i.e.*, with an incremented ion charge and a slowed down incident electron), the probability to extract one and only one electron reads

B. Stopping power

The slowing down of test electrons through an $e - i$ plasma is mainly due to (elastic and inelastic) $e - e$ collisions. Rohrlich and Carlson[35] provide an analytical formula of the stopping power (used in the NIST database[36]) that takes into account both the free and bound target electrons. Let us compare this widely used model with the stopping power resulting from the coupled elastic and inelastic collisional schemes of Secs. II and IV. To this goal, monokinetic electrons, with energies ranging from 10 eV to 10 MeV and density $n_b = 1 n_c$, are injected through cold neutral solid-density aluminum ($n_{Al} = 60 n_c$). The domain is comprised of 128 cells, with $N_e = N_i = 50$. The time-step is 2.8×10^{-3} fs. The stopping power is computed from the early time energy loss rate as explained in Sec. III B.

As shown in Fig. 6, the agreement between our collisional scheme and the analytical model of Ref. 35 is excellent over a broad energy range. The discrepancy arising at low energies stems from the fact that the analytical model is
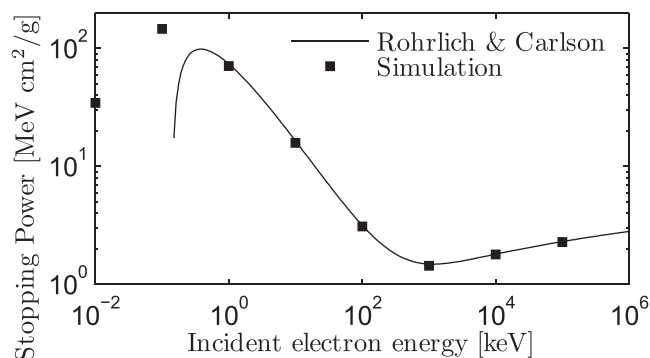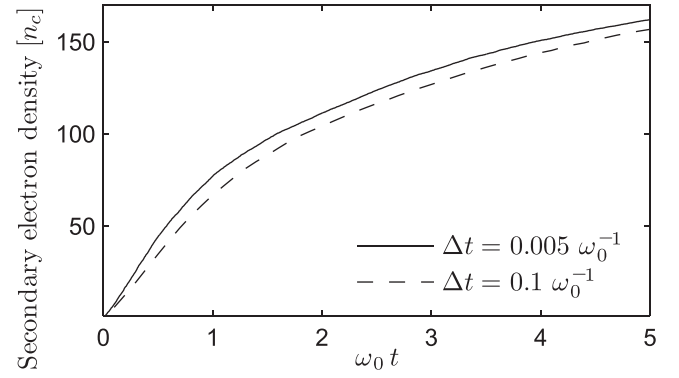

FIG. 6. Stopping power due to elastic and inelastic collisions for electrons in neutral solid Al: comparison between simulations and the analytical formulation of Ref. 35.

$$P_{\text{ioniz}}^1 = \left[\exp\left(-v_{\text{rel}} \frac{n_e n_i}{n_{ei}} \bar{\sigma}' \overline{\Delta t} \right) - \exp\left(-v_{\text{rel}} \frac{n_e n_i}{n_{ei}} \bar{\sigma} \overline{\Delta t} \right) \right]$$
$$\times \frac{\bar{\sigma}}{\bar{\sigma} - \bar{\sigma}'} , \qquad (36)$$

whereas the probability for two successive ionizations is

$$P_{\text{ioniz}}^2 = 1 - \frac{\bar{\sigma}}{\bar{\sigma} - \bar{\sigma}'} \times \left[\exp\left(-v_{\text{rel}} \frac{n_e n_i}{n_{ei}} \bar{\sigma}' \overline{\Delta t} \right) \right.$$
$$\left. - \frac{\bar{\sigma}'}{\bar{\sigma}} \exp\left(-v_{\text{rel}} \frac{n_e n_i}{n_{ei}} \bar{\sigma} \overline{\Delta t} \right) \right]. \tag{37}$$

The number of successive ionization events $k \in (0, 1, 2)$ occurring during a given time-step can then be sampled by inverting the cumulative distribution function[37]

$$F_{\text{ioniz}}^k = \sum_{j=0}^{k} P_{\text{ioniz}}^j, \tag{38}$$

where $P_{\text{ioniz}}^0 = \exp(-v_{\text{rel}} n_e n_i \bar{\sigma} \overline{\Delta t} / n_{ei})$. One can easily check that $F_{\text{ioniz}}^2 = 1$. As a consequence, given the random number $U \in [0; 1]$, the number of ionizations k is such that $F_{\text{ioniz}}^{k-1} < U \leq F_{\text{ioniz}}^k$ with $F_{\text{ioniz}}^{-1} = 0$.

D. Recombination and ionization equilibrium

As in Ref. 17, electron recombination of atomic shell vacancies is neglected in our ionization model. Since recombination acts to counterbalance ionization, our scheme is expected to overestimate the mean ion charge of a plasma at thermal equilibrium. We have checked that this shortcoming remains limited under typical simulation conditions. As a test scenario, we have chosen to compare the self-consistent average ion charge of a dense plasma observed after 0.5 ps with a Thomas-Fermi-like model.[26] This ps time-scale is relevant to simulations of ultra-intense laser-plasma interaction, as it may take a few 100 fs for the laser-accelerated electrons to reach the deepest (cold) regions of the target. The plasma, which consists of solid Al with equal-temperature Maxwellian electron and ion populations, is preionized in order to shorten the transition phase. The system is discretized over 128 cells with $N_e = N_i = 50$ initially. The time-step is set to $0.2\omega_0^{-1}$. Several cases are tested, corresponding to varying initial temperatures, and the mean ion charge is plotted vs time in Fig. 8. Following an initial rise, the mean ion charge is seen to rapidly saturate at a value depending on the plasma temperature. From that time on, the ion charge keeps increasing, albeit at a negligible rate compared to the simulation duration.
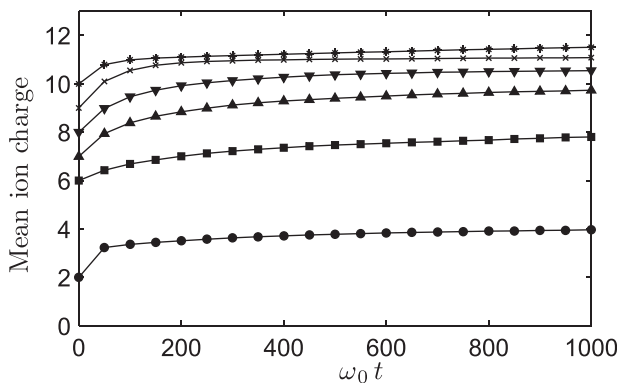

FIG. 8. Mean ion charge vs time of a preionized, solid-density Al plasma at thermal equilibrium in the absence of recombination. The different curves correspond to different final temperatures 14, 57, 122, 182, 437, and 854 eV, from bottom to top. Time is normalized to $\omega_0^{-1} = 0.53$ fs.
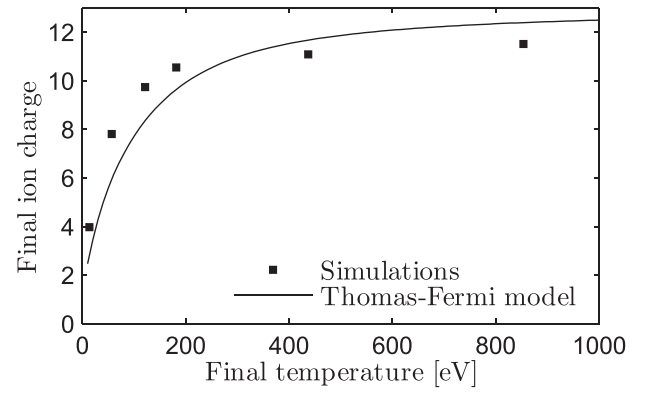

FIG. 9. Mean ion charge after 0.5 ps as a function of the final electron temperature. The model is taken from Ref. 26.

As a further check, Fig. 9 confronts, as a function of the final electron temperature, the saturated values of the mean ion charge of Fig. 8 to the theoretical predictions of Ref. 26. Overall, the simulations yield ionization values after 0.5 ps in satisfactory agreement with the model. The larger discrepancy occurs below 300 eV: the simulations then overestimate the model owing, probably, to the neglect of recombination. Yet, the difference remains tolerable regarding the required precision. The code slightly underestimates the Thomas-Fermi model at higher temperatures. As a result, electron recombination can, to first approximation, be ignored in PIC simulations of laser-irradiated dense plasmas.

VI. INTEGRATED SIMULATIONS

In the following, we illustrate the influence of elastic and inelastic collisions in the case of 1D × 3Dv (one-dimensional in space, three-dimensional in momentum) and 2D × 3Dv (two-dimensional in space, three-dimensional in momentum) CALDER PIC simulations of relativistic laser-plasma interaction.

A. Resistive fields

Self-generated resistive fields may be of considerable importance for the transport of intense fast-electron currents in dense materials.[28,38] Their self-consistent description in collisional PIC simulations therefore constitutes a significant step towards a complete modeling of high energy density physics.[2,7,39] Let us focus here on the generation of resistive fields induced by laser-driven currents in a 2D × 3Dv dense plasma. We consider a plasma slab irradiated by a normally incident laser pulse of 3×10^{19} W/cm² peak intensity, 100 fs rise-time and 10 μm-FWHM Gaussian transverse profile. The target consists of a solid-density ($\rho = 2.7$ g/cm³), 30 μm-thick Al^{3+} layer. An exponential preplasma is added in front of the target, the critical density being located 2 μm away from the solid-density region. The initial temperature is 10 eV. The system comprises 6000 × 10 000 cells with mesh sizes $\Delta x = \Delta y = 0.05 c/\omega_0$. The time-step is $\Delta t = 0.035\omega_0^{-1}$. For each species, 30 macro-particles per cell are used to initialize the plasma. Here, both elastic and inelastic collisions are modeled. Third-order weight factors are employed in order to keep the numerical heating at a tolerable level: at the time
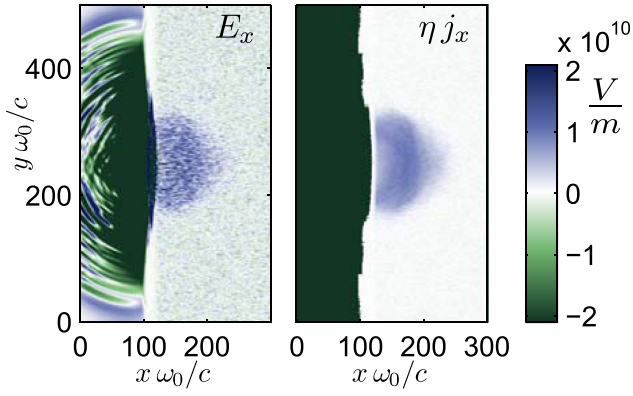
FIG. 10. Spatial distribution of the (laser cycle-averaged) electric field E_x (left) and of the product ηj_x (right) at $t = 200$ fs. Only the contribution of the low-energy (< 10 keV) electrons is accounted for in the current density. The target occupies the region $100 < \omega_0 x/c < 300$ and the laser is incoming from the left.

when the laser pulse impinges onto the target, the electron temperature has increased from 10 to ~ 15 eV. This heating remains much weaker than that, in the 0.1-1 keV range, induced by the fast electrons in the central part of the target (not shown).

The laser-driven fast electron current generates an electric field **E** inside the dense plasma, which, in turn, accelerates a return current **j** made of thermal, collisional electrons. In case of sufficiently high target resistivity η and diluted fast electrons, the simple Ohm's law $\mathbf{E} \approx \eta \mathbf{j}$ is expected to hold to first approximation.[28,40] To support this relation, its left- and right-hand sides are extracted from the PIC simulation after 200 fs, use being made of Eq. (26) to compute the electrical resistivity η from the measured temperature of the low-energy part (< 10 keV) of the electron population. The 2-D maps of the longitudinal (averaged over a laser cycle) electric field E_x and the product ηj_x are displayed in Fig. 10. Starting from the laser interaction zone, a region containing a positive electrical field extends inside the target bulk. This field matches well the predicted behavior ηj_x, which serves as evidence to its resistive character. Outside the target, the fields are driven by collisionless currents, and hence cannot be compared to ηj_x. As illustrated in Fig. 11, a resistive
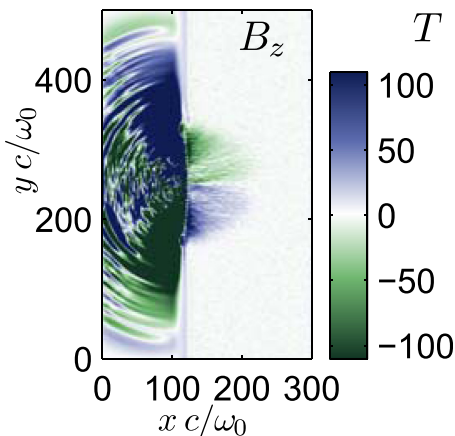
magnetic field B_z concomitantly builds up as a result of Faraday's law $\partial \mathbf{B}/\partial t = -\nabla \times \mathbf{E} \approx -\nabla \times (\eta \mathbf{j})$.

B. Energy loss through ionization

The effects of collisional ionization will now be demonstrated using another simulation. For this, let us simulate the irradiation of a 50 μm-thick solid Al^{3+} slab within a one-dimensional (1D $\times$ 3Dv) geometry. The system is comprised of 20 000 cells with $\Delta x = 0.02 c/\omega_0$. Each plasma cell initially contains 200 electrons and ions. The exponential preplasma present at the target front is such that the critical surface is located 3 μm away from the solid region. The initial temperature is 50 eV. The laser intensity increases linearly during 20 fs and then remains constant at 3×10^{19} W/cm^2 during 350 fs. The ions contained in the first 5 μm of plasma are kept immobile and at a fixed charge state in order to ensure a quasi-stationary fast-electron source.

The energetic electrons injected through the target are expected to yield a decreasing energy flux density vs distance as a result of (elastic and inelastic) collisions and resistive fields. The stopping power plotted in Fig. 6 thus predicts a typical 50 μm range for 100 keV electrons. Without ionization, elastic collisions also contribute to slowing down the fast electrons, but with a stopping power lower by a factor $Z^\star/Z$. We thus expect a more rapid decrease in the energy flux density with distance when ionization is included in the simulation.

Figure 12, which compares the results obtained with and without ionization, shows that the ionization effects indeed significantly reduce the fast-electron energy flux. Moreover, Fig. 13 indicates that the fast-electron-induced heating of the target bulk may be almost twice lower when account is made of ionization. These changes can be attributed to several factors including the variation of the laser absorption with the increasing target charge state, or the conversion of the fast-electron energy into ionization energy. Furthermore, upon comparing the spatial profiles of E_x, it is found that the ionization effects enhance the generation of the resistive electric field (Fig. 14). Again, we check the essentially resistive character of this field by plotting on the same graph of the product ηj_x.

FIG. 11. Spatial distribution of the (laser cycle-averaged) magnetic field B_z after 200 fs.
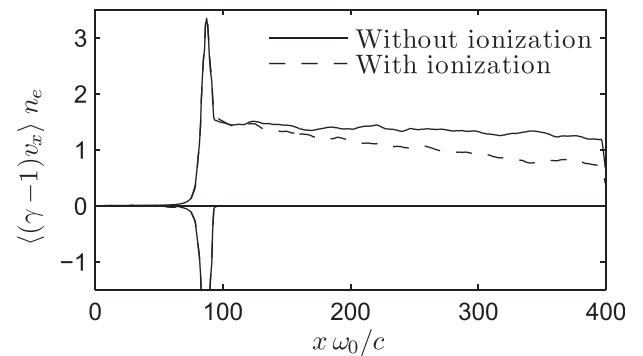

FIG. 12. Spatial profile of the energy flux density of the fast electrons (above 10 keV) at the end of the simulation. The positive and negative curves correspond to the forward- and backward-going electrons, respectively. The aluminum target is defined in the region $90 < \omega_0 x/c < 400$ and the laser is incoming from the left.
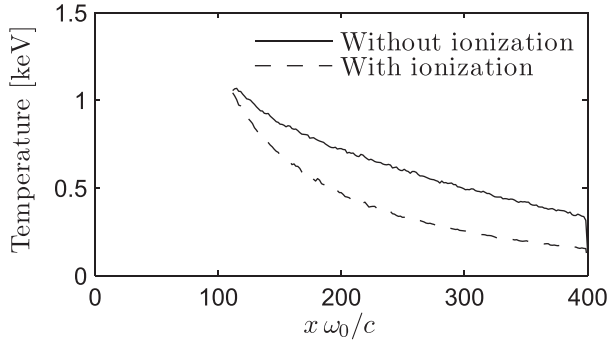
FIG. 13. Spatial profile of the thermal-electron ($<10\,\mathrm{keV}$) temperature at the end of the simulation.

In order to determine the dominant relaxation processes, we have carried out additional simulations (keeping a fixed laser intensity). The most salient results are the following: (1) the fast-electron source at the laser interaction region is significantly reduced by ionization. This explains why ionization was turned off around the interaction region in the previous example. (2) Ionization is the main process which cools down thermal electrons by converting their thermal energy into ionization energy. (3) The resistive electric field is enhanced by a factor $\sim 2-4$ with ionization because, in the Spitzer regime ($\gtrsim 50$ eV for solid-density Al, see Fig. 2), a lower plasma temperature implies a higher resistivity.

An overall picture of energy transport can be drawn from these findings. The fast electrons (typically $> 10\,\mathrm{keV}$) are slowed down through resistive fields and collisions. The former prevails for the laser and target parameters under consideration. This slowing down, stronger with ionization, induces a continuous heating of the bulk plasma. The ionization then mainly acts to convert the plasma thermal energy into ionization energy, resulting in approximately twice the lower plasma temperatures than in the absence of ionization. A second consequence is the varying target charge state which tends to increase the resistivity, and thus to amplify the slowing down from resistive fields. These features pinpoint the importance of accounting for ionization effects in laser-plasma configurations of experimental interest[7] and provide likely explanations for the overestimated target temperatures predicted in Ref. 2.
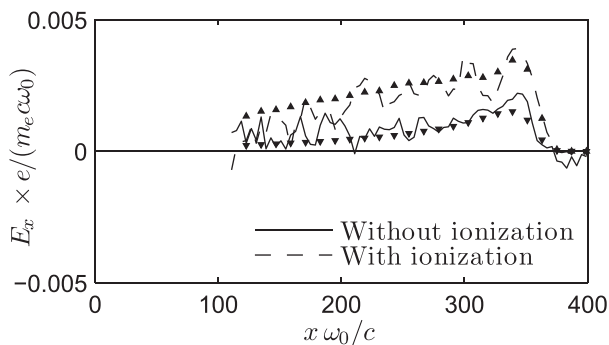

FIG. 14. Electric field E_x (laser cycle-averaged) with or without ionization after 200 fs in the simulation (solid and dashed lines). The triangles plot the expected resistive field ηj_x using Eq. (26) to calculate the resistivity.

VII. CONCLUSIONS

We have presented an improved Monte Carlo scheme for modeling elastic and inelastic collisions in PIC simulations using weighted macro-particles. Through the use of relativistic invariants, our scheme operates in the laboratory and center-of-mass frames only, hence providing a streamlined approach as compared to existing methods. Moreover, we propose an alternative low-temperature correction of the collision frequency suited to describing resistive effects in warm dense matter. Comparisons of the computed electrical conductivity and elastic stopping power with theoretical models prove the efficiency of our model in a wide parameter range. We have also implemented a binary collisional ionization scheme adapted to the relativistic regime and varying macro-particle weights. Test calculations demonstrate its ability to reproduce the theoretical inelastic stopping power of a solid-density plasma. Finally, we illustrate the modifications brought about by collisional effects in self-consistent PIC simulations of laser-driven fast-electron generation and transport. The resistive fields induced by the fast-electron current are found to affect the energy transport and to be sensitive to ionization.

[1] P. M. Nilson, A. A. Solodov, J. F. Myatt, W. Theobald, P. A. Jaanimagi, L. Gao, C. Stoeckl, R. S. Craxton, J. A. Delettrez, B. Yaakobi, J. D. Zuegel, B. E. Kruschwitz, C. Dorrer, J. H. Kelly, K. U. Akli, P. K. Patel, A. J. Mackinnon, R. Betti, T. C. Sangster, and D. D. Meyerhofer, Phys. Rev. Lett. **105**, 235001 (2010).

[2] F. Perez, L. Gremillet, M. Koenig, S. D. Baton, P. Audebert, M. Chahid, C. Rousseaux, M. Drouin, E. Lefebvre, T. Vinci, J. Rassuchine, T. Cowan, S. A. Gaillard, K. A. Flippo, and R. Shepherd, Phys. Rev. Lett. **104**, 085001 (2010).

[3] M. Tabak, J. Hammer, M. E. Glinsky, W. L. Kruer, S. C. Wilks, J. Woodworth, E. M. Campbell, M. D. Perry, and R. J. Mason, Phys. Plasmas **1**, 1626 (1994).

[4] R. A. Snavely, M. H. Key, S. P. Hatchett, T. E. Cowan, M. Roth, T. W. Phillips, M. A. Stoyer, E. A. Henry, T. C. Sangster, M. S. Singh, S. C. Wilks, A. MacKinnon, A. Offenberger, D. M. Pennington, K. Yasuike, A. B. Langdon, B. F. Lasinski, J. Johnson, M. D. Perry, and E. M. Campbell, Phys. Rev. Lett. **85**, 2945 (2000).

[5] H. Chen, S. C. Wilks, J. D. Bonlie, E. P. Liang, J. Myatt, D. F. Price, D. D. Meyerhofer, and P. Beiersdorfer, Phys. Rev. Lett. **102**, 105001 (2009).

[6] C. K. Birdsall and A. B. Langdon, *Plasma Physics via Computer Simulation* (Adam Hilger, Bristol, 1991).

[7] Y. Sentoku, E. D'Humières, L. Romagnani, P. Audebert, and J. Fuchs, Phys. Rev. Lett. **107**, 135005 (2011).

[8] R. Shanny, J. M. Dawson, and J. M. Greene, Phys. Fluids **10**, 1281 (1967).

[9] T. Takizuka and H. Abe, J. Comput. Phys. **25**, 205 (1977).

[10] J. M. Wallace, D. W. Forslund, J. M. Kindel, G. L. Olson, and J. C. Comly, Phys. Fluids B **3**, 2337 (1991).

[11] Y. Sentoku and A. J. Kemp, J. Comput. Phys. **227**, 6846 (2008).

[12] F. Peano, M. Marti, L. O. Silva, and G. Coppa, Phys. Rev. E **79**, 025701 (2009).

[13] E. Lefebvre, N. Cochet, S. Fritzler, V. Malka, M.-M. Aléonard, J.-F. Chemin, S. Darbon, L. Disdier, J. Faure, A. Fedotoff, O. Landoas, G. Malka, V. Méot, P. Morel, M. R. L. Gloahec, A. Rouyer, C. Rubbelynck, V. Tikhonchuk, R. Wrobel, P. Audebert, and C. Rousseaux, Nucl. Fusion **43**, 629 (2003).

[14] K. Nanbu, Phys. Rev. E **55**, 4642 (1997).

[15]K. Nanbu and S. Yonemura, J. Comput. Phys. **145**, 639 (1998).

[16]C. Wang, T. Lin, R. Caflisch, B. I. Cohen, and A. M. Dimits, J. Comput. Phys. **227**, 4308 (2008).

[17]A. J. Kemp, R. E. W. Pfund, and J. Meyer-ter-Vehn, Phys. Plasmas **11**, 5648 (2004).

[18]Y. Sentoku, K. Mima, Y. Kishimoto, and M. Honda, J. Phys. Soc. Jpn. **67**, 4084 (1998).

[19]L. D. Landau and E. M. Lifshitz, *The Classical Theory of Fields* (Butterworth-Heinemann, Burlington, 1975), p. 37.

[20]N. E. Frankel, K. C. Hines, and R. L. Dewar, Phys. Rev. A **20**, 2120 (1979).

[21]E. M. Lifshitz and L. P. Pitaevskii, *Physical Kinetics* (Butterworth-Heinemann, Oxford, 1981), p. 206.

[22]R. H. Miller and M. R. Combi, Geophys. Res. Lett. **21**, 1735, doi:10.1029/94GL01835 (1994).

[23]Y. T. Lee and R. M. More, Phys. Fluids **27**, 1273 (1984).

[24]K. Eidmann, J. Meyer-ter-Vehn, T. Schlegel, and S. Hüller, Phys. Rev. E **62**, 1202 (2000).

[25]A. Decoster, in *Modeling of Collisions*, edited by P. A. Raviart (Gauthier-Villars, Paris, 1998).

[26]M. P. Desjarlais, Contrib. Plasma Phys. **41**, 267 (2001).

[27]R. Redmer, Phys. Rev. E **59**, 1073 (1999).

[28]A. R. Bell, J. R. Davies, and S. M. Guerin, Phys. Rev. E **58**, 2471 (1998).

[29]J. Robiche and J. M. Rax, Phys. Rev. E **70**, 046405 (2004).

[30]J. A. Bearden and A. F. Burr, Rev. Mod. Phys. **39**, 125 (1967).

[31]A. C. Thompson, D. T. Attwood, E. M. Gullikson, M. R. Howells, J. B. Kortright, A. L. Robinson, J. H. Underwood, K.-J. Kim, J. Kirz, I. Lindau, P. Pianetta, H. Winick, G. P. Williams, and J. H. Scofield, *X-Ray Data Booklet* (Lawrence Berkeley National Laboratory, 2001).

[32]See http://www.chembio.uoguelph.ca/educmat/atomdata/bindener/elec-bind.htm for binding energy tables of various atoms.

[33]T. A. Carlson, C. W. Nestor, Jr., N. Wasserman, and J. D. McDowell, At. Data Nucl. Data Tables **2**, 63 (1970).

[34]Y.-K. Kim, J. P. Santos, and F. Parente, Phys. Rev. A **62**, 052710 (2000).

[35]F. Rohrlich and B. C. Carlson, Phys. Rev. **93**, 38 (1954).

[36]M. Berger, J. Coursey, M. Zucker, and J. Chang, "ESTAR, PSTAR, and ASTAR: Computer programs for calculating stopping-power and range tables for electrons, protons, and helium ions," National Institute of Standards and Technology, Gaithersburg, MD, 2005. Available at http://www.nist.gov/pml/data/star/version.cfm.

[37]R. Nuter, L. Gremillet, E. Lefebvre, A. Lévy, T. Ceccotti, and P. Martin, Phys. Plasmas **18**, 033107 (2011).

[38]A. R. Bell and R. J. Kingham, Phys. Rev. Lett. **91**, 035003 (2003).

[39]B. I. Cohen, A. J. Kemp, and L. Divol, J. Comput. Phys. **229**, 4591 (2010).

[40]M. Sherlock, Phys. Rev. Lett. **104**, 205004 (2010).